

# Plasma Membrane Reshaping during Endocytosis Is Revealed by Time-Resolved Electron Tomography

Wanda Kukulski,<sup>1,2</sup> Martin Schorb,<sup>1</sup> Marko Kaksonen,<sup>1,2,\*</sup> and John A.G. Briggs<sup>1,2,\*</sup>

<sup>1</sup>Structural and Computational Biology Unit

<sup>2</sup>Cell Biology and Biophysics Unit

European Molecular Biology Laboratory, Meyerhofstrasse 1, D-69117 Heidelberg, Germany

\*Correspondence: kaksonen@embl.de (M.K.), briggs@embl.de (J.A.G.B.)

<http://dx.doi.org/10.1016/j.cell.2012.05.046>

## SUMMARY

Endocytosis, like many dynamic cellular processes, requires precise temporal and spatial orchestration of complex protein machinery to mediate membrane budding. To understand how this machinery works, we directly correlated fluorescence microscopy of key protein pairs with electron tomography. We systematically located 211 endocytic intermediates, assigned each to a specific time window in endocytosis, and reconstructed their ultrastructure in 3D. The resulting virtual ultrastructural movie defines the protein-mediated membrane shape changes during endocytosis in budding yeast. It reveals that clathrin is recruited to flat membranes and does not initiate curvature. Instead, membrane invagination begins upon actin network assembly followed by amphiphysin binding to parallel membrane segments, which promotes elongation of the invagination into a tubule. Scission occurs on average 9 s after initial bending when invaginations are ~100 nm deep, releasing nonspherical vesicles with 6,400 nm<sup>2</sup> mean surface area. Direct correlation of protein dynamics with ultrastructure provides a quantitative 4D resource.

## INTRODUCTION

Clathrin-mediated endocytosis is one of the key transport pathways in eukaryotic cells (Brodsky et al., 2001; Conner and Schmid, 2003; McMahon and Boucrot, 2011). In clathrin-mediated endocytosis, the cell invaginates the plasma membrane and pinches off a small vesicle that is enclosed in a protein coat composed of clathrin with adaptor and accessory proteins. Clathrin-mediated endocytosis is involved in various cellular processes, including nutrient uptake, regulated recycling of plasma membrane components, and neural signaling.

The pioneering studies used electron microscopy (EM) to describe the basic concept of clathrin-mediated endocytosis (Anderson et al., 1977; Heuser, 1980; Roth and Porter, 1964). These ultrastructural studies were complemented by bio-

chemical and genetic studies that identified the proteins involved and dissected the molecular mechanisms. More than 50 different proteins act in clathrin-mediated endocytosis, forming a complex network of protein-protein and protein-lipid interactions (McMahon and Boucrot, 2011; Perrais and Merrifield, 2005). Most of the core protein components of the endocytic machinery are found throughout eukaryotes, suggesting that the basic mechanisms are highly conserved (Boettner et al., 2012).

Live-cell imaging of fluorescently tagged endocytic proteins has revealed the dynamic behavior of the endocytic machinery in high temporal resolution. The different proteins form functional modules, which are involved in different stages of endocytosis and are recruited to the endocytic site with a regular order (Kaksonen et al., 2005; Taylor et al., 2011). These experiments define the temporal sequence during the average endocytic event in yeast. The early module, which includes clathrin, scaffold protein Ede1, and several adaptor proteins (Stimpson et al., 2009), initiates assembly. This phase ends when late coat module proteins, including Sla1 and actin nucleation regulators such as yeast WASP Las17, are recruited, remaining at the site for ~30 s. On average, 15–20 s after assembly of these proteins, a short burst of actin polymerization occurs. Approximately 3 s after actin polymerization is initiated, scission module proteins (the N-BAR-domain-containing amphiphysins Rvs161 and Rvs167) are recruited for ~10 s, during which the vesicle separates from the plasma membrane (Kaksonen et al., 2005; Kukulski et al., 2011). Finally, ~3 s after Rvs167 departure, actin can no longer be detected, and the endocytic machinery has been disassembled. Although the lengths of each stage can vary between different endocytic sites, the order in which proteins arrive or depart has been shown to be essentially invariant for several protein pairs. Ede1 has been observed to always arrive before Sla1 (Toshima et al., 2006); Sla1 always arrives before Abp1 (Kaksonen et al., 2003); Abp1 always arrives before Rvs167 (Kaksonen et al., 2005); Rvs167 has been observed to always arrive before Sla1 departs (Kaksonen et al., 2005); and Sla1 and Rvs167 have been found to always depart before Abp1 departs (Kaksonen et al., 2003, 2005).

Although a lot is known about the composition and function of the endocytic machinery, how endocytic proteins shape the membrane from a flat sheet into a vesicle is still not understood.

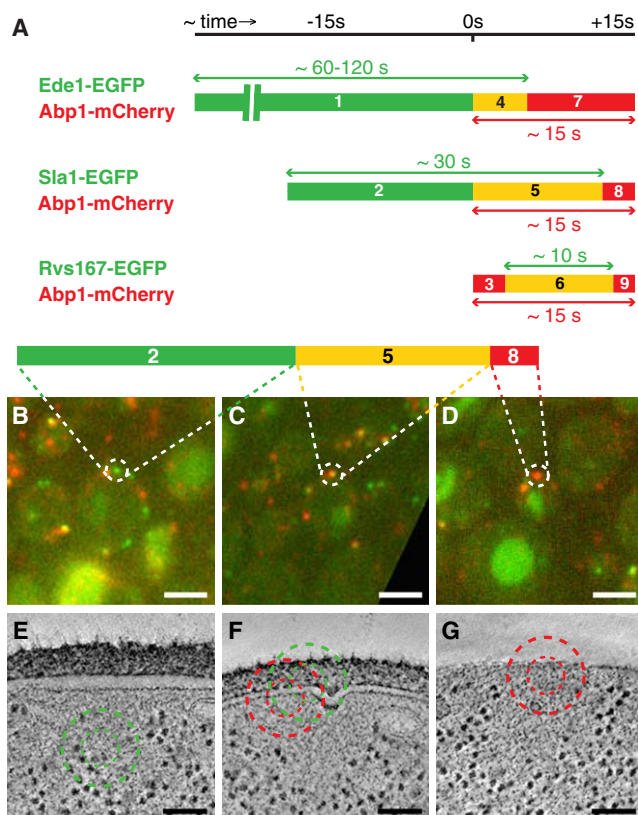


**Figure 1. Experimental Design**

(A) The three *S. cerevisiae* strains used in this study express Ede1-EGFP/Abp1-mCherry, Sla1-EGFP/Abp1-mCherry, and Rvs167-EGFP/Abp1-mCherry. The lengths of the green, yellow, and red bars represent the average lifetimes of fluorescent spots with the corresponding color in each strain, and each bar defines a time window numbered as indicated. Because the arrival of Abp1-mCherry is the shared reference time point of the three strains, it is assigned to  $T = 0$  s in the timeline (black line).

(B–D) Overlays of GFP and red fluorescent protein (RFP) signals of 300 nm sections of resin-embedded yeast cells expressing Sla1-EGFP and Abp1-mCherry, placed on EM grids. A green fluorescent spot is marked in (B), a colocalizing spot in (C), and a red spot in (D), corresponding to time windows 2, 5, and 8, respectively.

(E–G) Slices through electron tomograms taken at the marked positions show the corresponding ultrastructures underlying the fluorescent spots. Inner and outer circles mark 50% and 80% prediction accuracy for mCherry (red) and EGFP (green). Scale bars, 2  $\mu$ m in (B)–(D) and 100 nm in (E)–(G).

Several proteins, including clathrin, epsins, and BAR domain proteins, have been suggested to contribute to changing the preferred curvature of the membrane (Boettner et al., 2009; Ford et al., 2002; Henne et al., 2010; Hinrichsen et al., 2006; Itoh et al., 2005; Peter et al., 2004). Further, polymerization of actin at the endocytic site may provide force to reshape the membrane (Collins et al., 2011; Cureton et al., 2010). How the vesicle is pinched off is also unclear. The GTPase dynamin is thought to drive this scission in mammalian cells (Pucadyil and Schmid, 2008), but alternative mechanisms such as lipid-domain-induced line tension or actin polymerization have been suggested and must, at least in yeast, act in the absence of dynamin (Liu et al., 2006; Yasar et al., 2005).

The plasma membrane is not only a substrate of the endocytic machinery but is itself a core part of the machinery, passing information between proteins that influence membrane curvature and proteins that sense it. To reach a systems-level mechanistic understanding of endocytosis, it is necessary to link the biochemical, genetic, and dynamic fluorescence microscopy (FM) data, with information on the membrane shape at each stage in the process. This would permit changes in membrane curvature to be correlated with the presence or absence of particular proteins and could inform models of force distribution on the membrane. Due to the small size of endocytic structures, this shape can only be obtained by using EM, but it is challenging to apply EM to defined dynamic endocytic intermediates, and therefore, much of the ultrastructural data have been difficult to interpret functionally. Here, we have systematically applied our recent correlative FM and EM method (Kukulski et al., 2011) to study clathrin-mediated endocytosis in yeast, directly linking protein composition with plasma membrane shape and ultrastructure at the key steps of endocytosis. These data define the most important functional transitions along the path from a flat membrane to a free vesicle. This information forms a basis to build quantitative and mechanistically predictive models of vesicle budding.

## RESULTS

### Experimental Design

Endocytic proteins are recruited to and dissociate from the budding site in a defined temporal order. Thus, by attaching fluorescent tags to certain key proteins, it is possible to specifically label a sequence of time windows during endocytosis. We selected Ede1, a component from the early module; Sla1, a component of the coat module; and Rvs167, a component of the amphiphysin module, and we generated three *Saccharomyces cerevisiae* strains expressing enhanced green fluorescent protein (EGFP)-tagged variants of these proteins. In all three strains, Abp1, a component of the actin module, was tagged with mCherry. In the Ede1-labeled strain, for example, early stages in endocytosis are green; at middle stages, red and green colocalize; and late stages are red. Together, the three strains allow us to identify nine overlapping time windows in endocytosis by their fluorescent signal (Figures 1 and 2A). Although the lengths of these time windows vary between endocytic sites, their temporal order does not (Kaksonen et al., 2003, 2005; Toshima et al., 2006).

We recently described a correlative FM and EM method that permits faint fluorescent signals from green fluorescent protein (GFP)- or mCherry-tagged proteins to be localized in electron tomograms with a precision better than 100 nm (Kukulski et al., 2011). The method builds on the finding that GFP signals can be preserved in resin-embedded cells (Nixon et al., 2009). We applied this method to our three labeled yeast strains. In all cases, labeled endocytic intermediates were clearly identified as fluorescent spots and could be assigned to one of the time windows (Figures 1B–1D). The correlative method allowed us to image the corresponding areas by electron tomography (ET) (Figures 1E–1G). The high spatial precision of the correlation (Figures 1E–1G and Figure S1 available online) permits positive

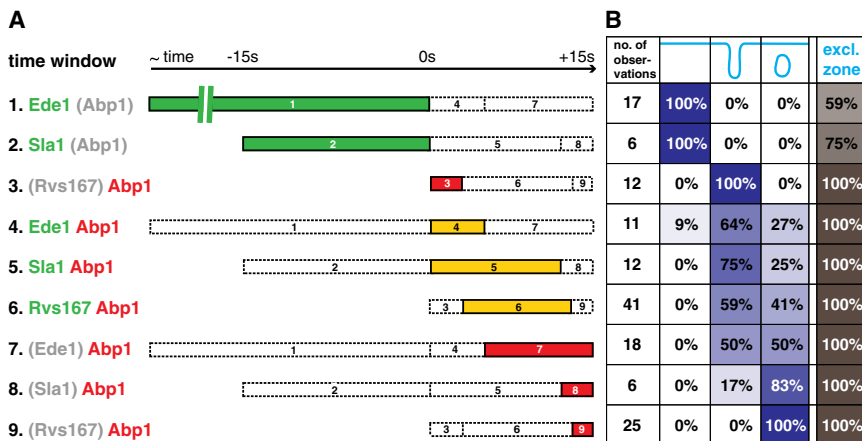


**Figure 2. Occurrence of Membrane Ultrastructures per Time Window**

(A) The nine time windows and their temporal arrangement relative to each other.

(B) The number of observations in each time window (first column), the percentage of observations showing flat membranes (second column), plasma membrane invaginations (third column), vesicles (fourth column), and a cytoplasmic zone excluding ribosomes near the endocytic membrane (fifth column). The strength of the shading corresponds to the percentage.

identification of endocytic events, distinguishing them unambiguously from other membrane invaginations such as furrows or fusing exocytic vesicles, as well as from other vesicles (Figure S2).

We generated a data set containing 148 three-dimensional (3D) electron tomographic reconstructions of endocytic intermediates. Based on its respective fluorescent signal, we assigned each to one of the nine defined time windows. In this manner, the endocytic protein machinery itself is used as an experimental clock, which is functionally linked to the underlying changes in membrane shape.

### Correlating Changes in Membrane Shape with Time and Protein Composition

The 148 endocytic intermediates subdivide into 62 invaginations of various depths, 62 vesicles, and 24 intermediates in which no plasma membrane ultrastructure comparable to the endocytic invaginations or vesicles was found, and which we class as flat plasma membranes. We quantified the occurrence of these different classes within each of the nine time windows (Figure 2B).

Where the early module or coat module is present at the endocytic site, but where actin assembly has not yet begun (time windows 1 and 2,  $n = 23$ ), we found only flat plasma membranes within the predicted signal localization (Figures 3A and 3B). After the initiation of actin polymerization (time windows 3–9,  $n = 125$ ), >99% of sites showed either an invagination or a vesicle. Membrane curvature is thus not initiated at the point of coat recruitment but rather when actin polymerization begins at the endocytic site.

To substantiate this observation, we used Latrunculin A to hinder actin polymerization in cells expressing Sla1-EGFP and Abp1-mCherry. Latrunculin-A-treated cells showed immobile Sla1 spots and lacked distinct Abp1 spots, indicating that actin patches were not formed and coat internalization could not occur (Kaksonen et al., 2003). We collected electron tomograms at the locations of 19 Sla1-EGFP spots (Figure S3). We observed no endocytic invaginations, confirming that induction of endocytic membrane curvature is coupled to actin polymerization.

Within time windows 4–8, both invaginations and free vesicles were observed but with different proportions in different time

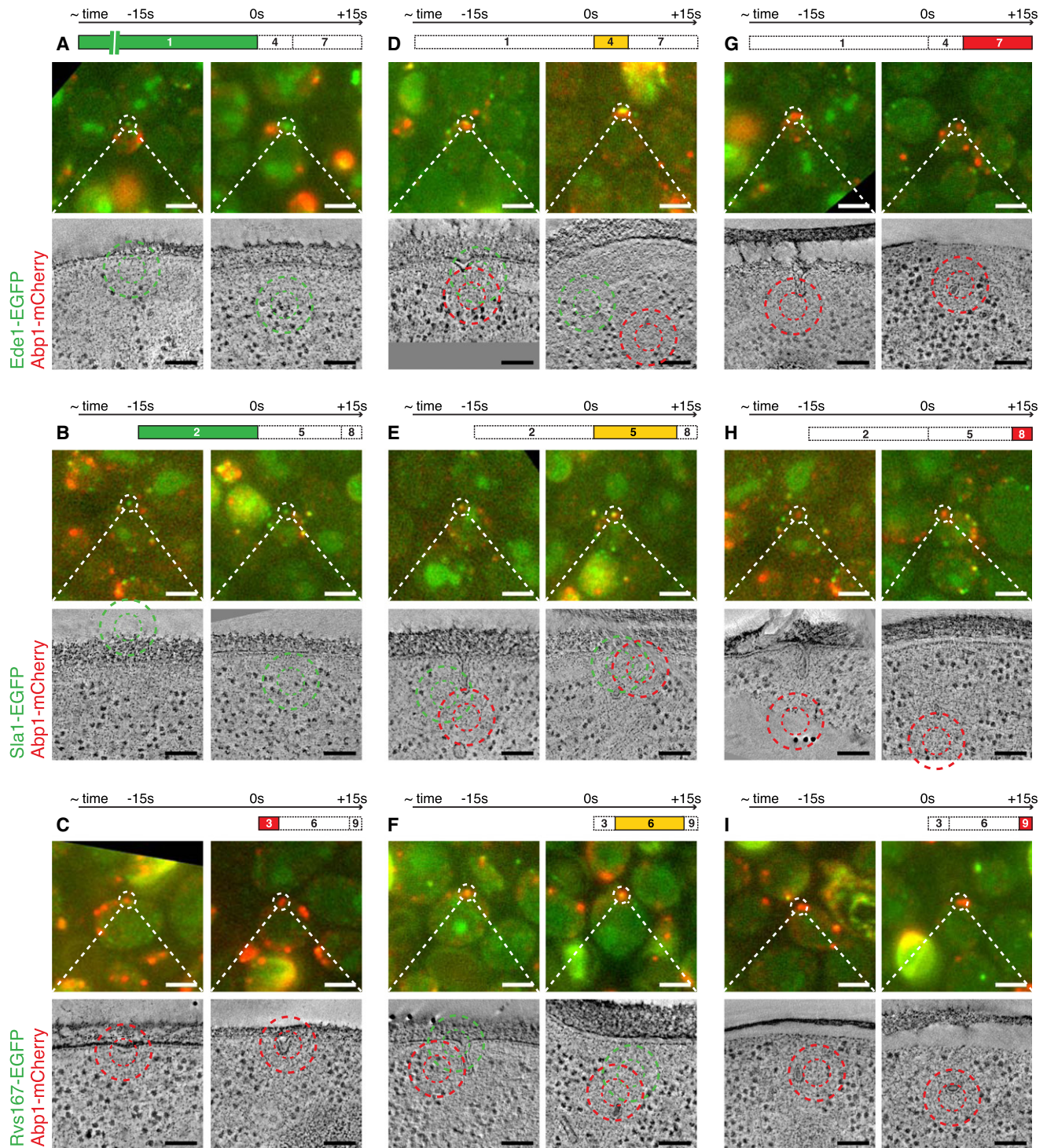
0%	17%	83%	100%
0%	0%	100%	100%

In time window 4 ( $n = 11$ ), where Abp1 and Ede1 are both present, we found 64% invaginations and 27% vesicles (Figure 3D) (as well as one flat plasma membrane, which may represent a moment very shortly after initiation of actin polymerization, when the plasma membrane has not yet started to bend). In time window 7 ( $n = 18$ ), where Abp1 is present at the site, but Ede1 has already departed, we found 50% invaginations and 50% vesicles (Figure 3G), implying that Ede1 can leave the endocytic site before or after scission. Ede1 has been described to have variable lifetimes (Stimpson et al., 2009), but its departure relative to the other endocytic markers Sla1, Abp1, and Rvs167 has not been quantified. Our data indicate that the early module is not required at the endocytic site during scission and neither is its departure a prerequisite for scission.

Time windows 3 and 9 are both identified as red spots in the Abp1-mCherry/Rvs167-EGFP strain and can therefore not be distinguished based only on fluorescence signal. They are temporally separated by time window 6, where both Abp1 and Rvs167 are present at the endocytic site. Time window 6 contained only deep (late) invaginations or vesicles (see below). Time windows 3 and 9 ( $n = 37$ ) contained exclusively shallow (early) invaginations (32%) or vesicles (68%), allowing us to assign the early invaginations to time window 3 and the vesicles to time window 9 (Figures 3C and 3I). Within time window 6 ( $n = 41$ ), we observed 59% invaginations and 41% vesicles (Figure 3F), indicating that scission occurs on average after 59% of the Rvs167 lifetime, which is about 10 s (Kaksonen et al., 2005). Thus, scission takes place on average about 6 s after Rvs167 recruitment has started, and Rvs167 remains at the endocytic site for about 4 s after scission.

The moments immediately after scission are represented by the 62 endocytic vesicles in our data set. For none did we observe any indentation remaining on the plasma membrane in the vicinity of the vesicles. We can estimate that  $\sim 25$  of these vesicles were frozen within 4 s of scission (see [Extended Experimental Procedures](#)), implying that the plasma membrane relaxes to a flat state rapidly after scission (the posterior mean





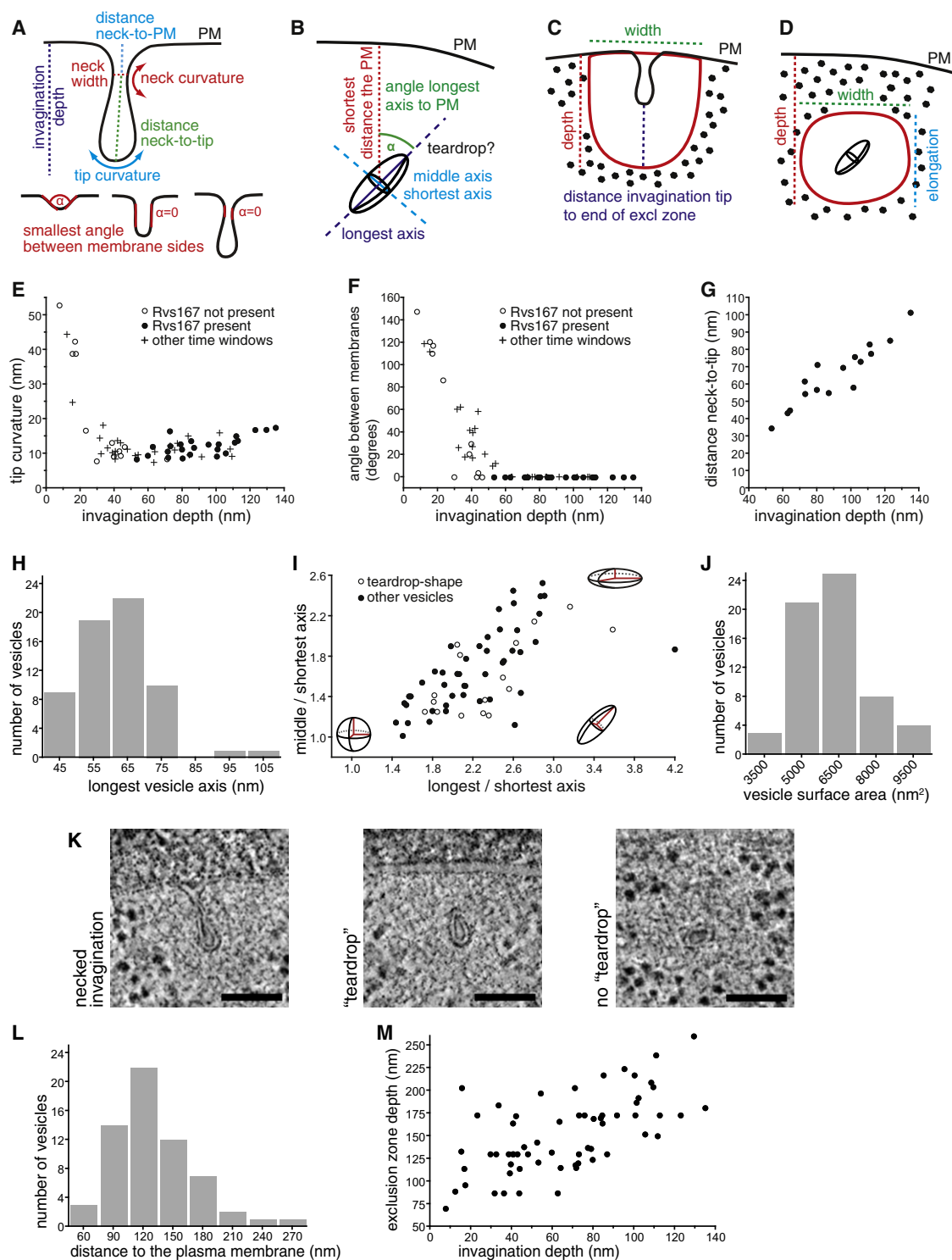


**Figure 4. Quantitative Analysis of the Parameters Extracted from Membrane Ultrastructures**

(A) Schematic of a plasma membrane invagination and parameters obtained from measurements on its profile. The lower panel illustrates the definition of the minimal angle between the sides of the invagination profile.

(B) Schematic of a vesicle and the parameters obtained from the ellipsoid fit of the vesicle.

(C and D) (C) Schematic of parameters measured from exclusion zones that are connected to the plasma membrane (invaginations and vesicles) and (D) from exclusion zones that are disconnected from the plasma membrane (vesicles). For detailed definitions of parameters, see [Extended Experimental Procedures](#).

(E) Invagination depth versus tip curvature.

for the membrane relaxation time is 150 ms; for calculations, see [Extended Experimental Procedures](#)).

Because we used Abp1-mCherry as a marker for late stages of endocytosis, all of the vesicles in the data set are imaged prior to actin disassembly. No vesicles were interacting with other membrane compartments, indicating that the departure of the surrounding actin cytoskeleton from the endocytic vesicle always occurs before it fuses with an endosome.

### Quantitative Analysis of Membrane Shapes

We next carried out a quantitative analysis of membrane shapes during endocytosis. We extracted the membrane profile from each tomogram as a line fitted through a series of  $x$  and  $y$  coordinates on a plane along the major axis of the invagination. The outline of the exclusion zone, a ribosome-free-zone surrounding both invaginations and vesicles (see below), was also recorded. From these data, we extracted nine parameters describing each invagination or vesicle ([Figure 4](#)). The parameter values, FM images, and tomograms for all endocytic intermediates are available at <http://www.embl.de/download/briggs/endocytosis.html>.

Endocytic invaginations appeared either as dome-shaped, shallow invaginations or longer, tubular invaginations, some of which had a neck-like constriction (for examples, see [Figure 3](#) and <http://www.embl.de/download/briggs/endocytosis.html>). They showed variable depth and variable membrane curvatures at neck and tip. The shallowest invagination that could be distinguished from a flat membrane had a depth of 8 nm, whereas the deepest protruded 135 nm into the cytoplasm. With the exception of time windows 4 and 7, whose end and beginning, respectively, are defined by the irregular departure of Ede1, there was a correlation between time window and invagination depth; later time windows showed deeper invaginations ([Figure S4](#)). Eleven of the 12 invaginations in time window 3 (prior to Rvs167 recruitment) were below 50 nm in depth, whereas all 24 invaginations in time window 6 (after Rvs167 recruitment) were deeper than 50 nm, suggesting that Rvs167 is recruited when the invagination depth reaches  $\sim 50$  nm.

Small invaginations appeared as shallow, dome-shaped dents in the plasma membrane. The curvature of the invagination tip increased with invagination depth until it plateaued at a tip curvature of  $\sim 12$  nm radius and a depth of  $\sim 40$  nm ([Figure 4E](#)).

We observed that deeper invaginations had undergone a transition from a dome shape to a tubular shape. To monitor this transition, we measured the smallest angles enclosed by the two faces on the invagination profile. For tubular invaginations, or those showing a neck-like constriction, this angle is 0 degrees, whereas for shallow invaginations, it tends toward 180 degrees ([Figure 4A](#)). As predicted, the angle decreased

with increasing invagination depth. At a depth of  $\sim 50$  nm, parallel membranes were formed, indicating the presence of a tubular segment ([Figure 4F](#)). Time window 6 contained only invaginations with parallel membranes, indicating that Rvs167 is only present on invaginations with parallel membranes and a depth of at least 50 nm ([Figure 4F](#)). Five of the 12 invaginations in time window 3 (prior to Rvs167 recruitment) had parallel membranes, suggesting that parallel membranes form before Rvs167 is recruited to the emerging tubule.

Of those invaginations containing parallel membranes ( $n = 40$ ), 40% had a clear constriction forming a neck, but the presence or absence of the neck did not correlate with invagination depth. We measured the Gaussian curvature of the membrane at the neck, the neck width, and the position of the neck relative to the plasma membrane and the invagination tip. Neither neck width nor neck curvature showed any significant correlation with depth. If a neck was present, its distance from the tip was consistently 2/3 of the invagination depth ([Figure 4G](#)).

### Shape and Position of Endocytic Vesicles

The endocytic vesicles in the data set were rather uniform in size but remarkably variable in shape, appearing elongated or flattened instead of being spherical. This contrasted with the almost spherical shapes of other cytoplasmic, nonlabeled vesicles observed in the tomograms ([Figures S2E and S2F](#)). To define the dimensions of the endocytic vesicles, we fitted them with an ellipsoid and measured the length of the three orthogonal axes. The longest axis was on average  $61.8 \pm 10.9$  nm ( $n = 62$ ) in length ([Figure 4H](#)), and the shortest was  $28.1 \pm 5.8$  nm ( $n = 62$ ). The short axes of the vesicles were randomly oriented and were not related to the plane of the section or to the section cutting direction. The ratios between the three orthogonal axes define the shape of the vesicles, which ranged from flattened spheres with axes ratios of up to 2.7:2.5:1.1 to elongated rugby-ball-shaped structures with axes ratios of 2.7:1.2:1 ([Figure 4I](#)). The most spherical endocytic vesicles still deviated from perfect spheres, with axes ratios of 1.4:1.1:1. Overall, the distribution suggests a continuous population of ellipsoid vesicles with three different axes lengths. The vesicles had a mean surface area of  $6,400 \pm 1,900$  nm<sup>2</sup> ( $n = 62$ ) ([Figure 4J](#)), and a mean volume of  $43,000 \pm 24,000$  nm<sup>3</sup> ( $n = 62$ ). The volume is thus reduced by about 10% compared to a sphere of the same surface area.

We noticed that 26% of endocytic vesicles exhibited a teardrop shape—rounded on one side and tapering to a point on the other. The point was oriented toward the plasma membrane in 81% of the cases (total  $n = 16$ ) ([Figure 4K](#)). These vesicles appeared to retain the shape of the invagination at the point of scission ([Figure 4K](#)). The teardrop shape did not correlate with

(F) Invagination depth versus minimal angle between membrane sides. In (E) and (F), open circles indicate Rvs167 absence (time window 3), and closed circles indicate Rvs167 presence (time window 6), whereas crosses indicate that the invagination belongs to time window 4, 5, 7, or 8.

(G) Invagination depth versus distance neck to tip.

(H) Histogram showing the distribution of the vesicles' longest axis length.

(I) Ratio of the vesicles longest-to-shortest axis versus ratio of the middle-to-shortest axis. Open circles indicate teardrop-shaped vesicles, and closed circles indicate other vesicles. Schemes depict the shapes at the given positions in the plot.

(J) Histogram showing the distribution of vesicles' surface area.

(K) Gallery illustrating the resemblance of teardrop-shaped vesicles to necked invaginations, as compared to non-teardrop-shaped vesicles. Scale bars, 100 nm.

(L) Histogram showing the distribution of the shortest distance between the vesicle center and the plasma membrane.

(M) Invagination depth versus the depth of the exclusion zone.



presence or absence of Rvs167. This suggests that teardrop-shaped vesicles are not exclusively observed during the period after scission when Rvs167 is still present and, therefore, that the shape is maintained for a number of seconds after scission.

Almost all vesicles in the data set were within 200 nm of the plasma membrane (Figure 4L), indicating that endocytic vesicles remain within a zone close to the plasma membrane while associated with Abp1.

### The Actin Network

Both invaginations and vesicles were surrounded by an “exclusion zone,” in which the cytoplasm was free of ribosomes. Previous immuno-EM studies showed that a zone around invaginations and vesicles in yeast contains actin and Abp1, and the zone was therefore interpreted as actin meshwork (Idrissi et al., 2008; Mulholland et al., 1994; Takagi et al., 2003). In our data, all sites with Abp1 present exhibited an exclusion zone, whereas during time windows 1 and 2, some, but not all, sites exhibited exclusion zones (Figure 2B). These observations are consistent with ribosome exclusion being caused by the endocytic machinery and, in particular, the dense actin network surrounding invaginations and vesicles. The exclusion zone expanded approximately evenly in all directions, unlike the laterally asymmetric actin network observed, and attributed a role during scission in mammalian cells (Collins et al., 2011).

We analyzed the exclusion zones to assess how changes of the actin network relate to membrane shape and topology. The exclusion zone reached  $\sim 86 \pm 33$  nm ( $n = 62$ ) further into the cytoplasm than the invagination tip. The depth and estimated volume of the exclusion zone grew with increasing invagination depth at approximately the same rate, suggesting continued growth of the actin network during invagination (Figure 4M). For the longest invaginations ( $>100$  nm), the exclusion zone extended  $193 \pm 32$  nm into the cytoplasm and had an average volume of  $\sim 0.003$  fl ( $n = 13$ ).

Vesicles were also surrounded by an exclusion zone. For 70% of vesicles, the zone extended to the plasma membrane. These vesicles were on average closer to the plasma membrane than the 30% of vesicles whose exclusion zone did not reach the plasma membrane ( $116 \pm 31$  nm [ $n = 44$ ] versus  $163 \pm 40$  nm [ $n = 18$ ],  $p < 0.0001$ ). This indicates that, at some point after scission, the exclusion zone detaches from the plasma membrane. The volume of vesicle exclusion zones that reached the plasma membrane ( $\sim 0.005$  fl) was larger than those that did not ( $0.003$  fl) and was larger than those around the longest invaginations ( $0.003$  fl), suggesting that the actin network continues to expand after scission until it disconnects from the plasma membrane.

### Endocytosis in RVS167-Deleted Cells

To further explore the role of Rvs167 during endocytosis, we studied cells of a mutant strain lacking the *RVS167* gene (*rvs167Δ*) and expressing Sla1-EGFP/Abp1-mCherry (Figures 5A–5D). Deletion of *RVS167* does not change the invariant order of arrival of Sla1 and Abp1 (Kaksonen et al., 2005). Observed by FM, most endocytic events in the *rvs167Δ* strain appear to internalize normally, but in about 25% of events, internalization of Sla1 patches is followed by a retraction movement that could represent failed scission (Kaksonen et al., 2005; Kishimoto

et al., 2011). In our correlative analysis of the *rvs167Δ* strain, time window 2 (prior to Abp1 recruitment) contained only flat membranes ( $n = 7$ ) as we had observed for wild-type cells. Signals corresponding to time window 5 ( $n = 30$ ) contained 57% invaginations and 37% vesicles, as well as two flat membranes. Time window 8, after Sla1 departure, contained only vesicles (Figure 5E). These observations confirm that endocytic sites proceed through scission in *rvs167Δ* cells. Surprisingly, the invaginations were, on average, shorter than in wild-type cells (mean depth:  $19 \pm 15$  nm ( $n = 17$ ) versus  $52 \pm 27$  nm ( $n = 9$ ) for time window 5 in wild-type cells,  $p = 0.0005$ ). They ranged in depth from 6 to only 62 nm with a striking accumulation of invaginations below 30 nm depth (Figure 5F). Two invaginations had parallel membrane segments (Figure 5F). These observations indicate that, in the absence of Rvs167, parallel membranes can form, but elongation of the tubular segments is hindered. Consistent with this observation, vesicles in the *rvs167Δ* mutant were significantly smaller than in wild-type cells (Figures 5G and 5H) with an average longest axis of  $52.1 \pm 8.7$  nm ( $n = 18$ ) and mean surface area of  $5,000 \pm 1,300$  nm<sup>2</sup> ( $n = 18$ ) ( $p = 0.0009$  and  $p = 0.0074$  compared to wild-type, respectively). 28% ( $n = 18$ ) of the vesicles had a teardrop shape.

## DISCUSSION

We have applied a correlative microscopy pipeline to establish systematic, time-resolved 3D ET of a dynamic process. Directly correlating protein dynamics with ultrastructural data on membrane dynamics gives a quantitative four-dimensional (4D) description of an average endocytic event and provides a resource for analysis of how proteins can dynamically shape membranes in vivo.

### Membrane Bending Is Initiated after Actin Polymerization Starts

Previous models suggest that initial bending of the plasma membrane occurs before the assembly of the actin network. Proteins present at the endocytic site prior to actin recruitment include clathrin, the ENTH-domain-containing epsins, and the F-BAR-domain-containing Syp1 (Boettner et al., 2009; Carroll et al., 2012; Kaksonen et al., 2005; Newpher et al., 2005; Stimpson et al., 2009). Both Syp1 and epsins can induce liposome tubulation in vitro (Ford et al., 2002; Reider et al., 2009). All of these proteins have previously been implicated as the initiators of membrane curvature (Ford et al., 2002; Galletta et al., 2010; Hinrichsen et al., 2006; Reider et al., 2009). Previous models were supported by data from immuno-EM, in which no Abp1 labeling and only minimal actin labeling was detected on invaginations below 50 nm depth (Idrissi et al., 2008). The correlative method applied here, likely reflecting higher sensitivity than the immuno-EM, shows that Abp1 is associated with all shallow invaginations, even the smallest ones with depths of only 8 nm. In contrast, the plasma membrane is flat prior to actin module recruitment. Further, in the presence of Latrunculin A, which inhibits actin polymerization, no endocytic invaginations were observed. These data imply that, in yeast, the proteins present at the endocytic site prior to actin recruitment are all unable to bend the membrane until actin polymerization begins. These

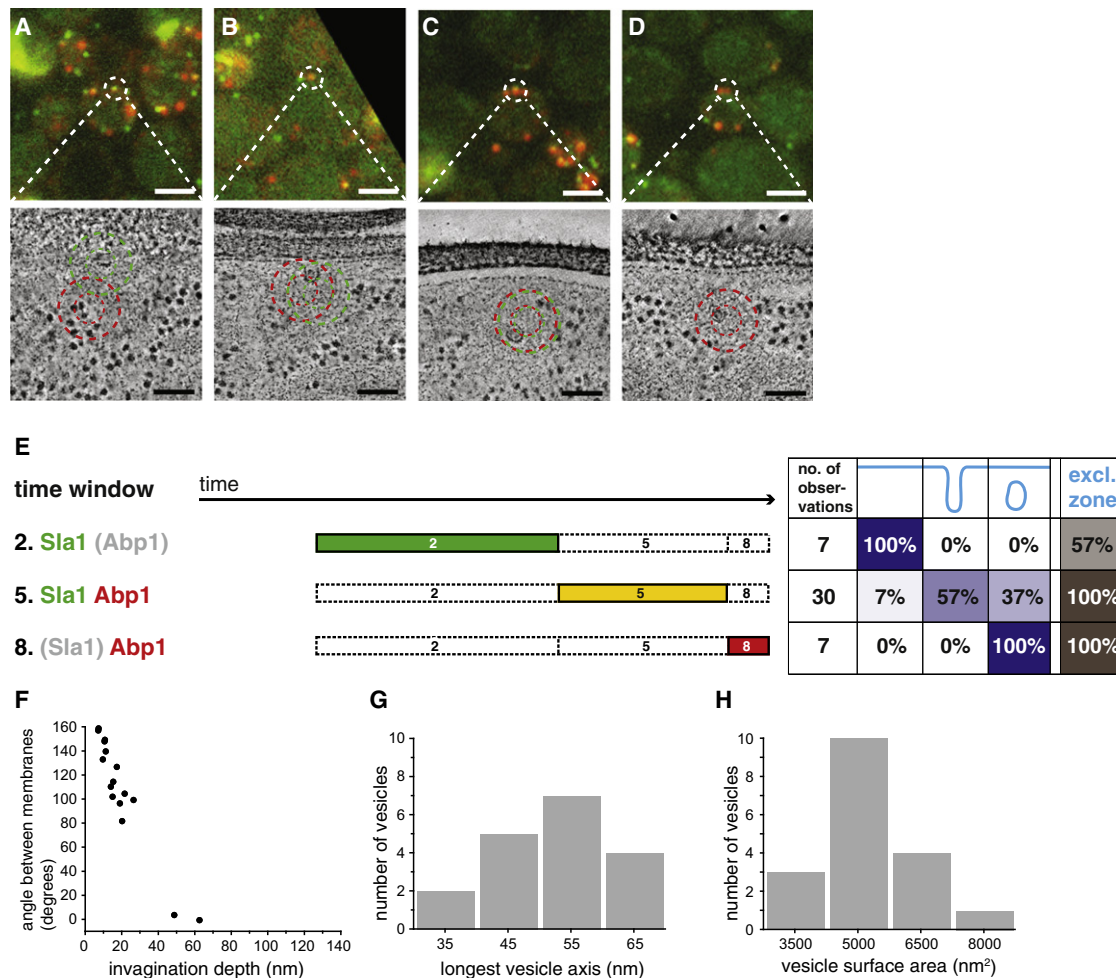


**Figure 5. Endocytic Ultrastructures in *rvs167Δ* Cells Expressing Sla1-EGFP and Abp1-mCherry and Quantitative Analysis**

(A–D) Example gallery of ultrastructures found at the position of colocalizing Sla1-EGFP/Abp1-mCherry signals (A–C) and an Abp1-mCherry signal (D). Scale bars in fluorescent images, 2  $\mu$ m; scale bars in electron tomographic slices, 100 nm.

(E) Occurrence of membrane ultrastructure per time window as in Figure 2.

(F) Invagination depth versus the minimal angle between membrane sides.

(G) Histogram showing the distribution of the vesicles' longest axis length.

(H) Histogram showing the distribution of the vesicles' surface area.

proteins must instead be assigned roles in sensing or modulating membrane curvature. Only upon actin recruitment to the site is sufficient force generated to counteract the cell's turgor pressure and bend the membrane into a dome-like clathrin-coated pit structure.

### Growth of the Invagination

After initiation of membrane bending, the curvature at the invagination tip increased until it reached  $\sim 12$  nm radius at  $\sim 40$  nm invagination depth. Proteins of the coat module have previously been shown to localize to the first 30 nm from the invagination tip (Idrissi et al., 2008), and it has been suggested that clathrin forms a hemisphere on the invagination tip rather than a full cage (Sirotkin et al., 2010). Our observations are consistent with a model in which, during actin-mediated increase of invagination depth from 0 to 40 nm, the coat arranges on the tip. After this point,

the shape of the tip with an average curvature of 12 nm is maintained by a hemisphere of assembled coat proteins.

Clathrin is therefore present on the membrane prior to the transition from a flat membrane to a highly curved invagination tip. This observation does not support a prevalent model in which the coat is assembled by stepwise addition of soluble clathrin triskelions to a growing curved clathrin lattice, which is concomitant with curvature of the membrane (Kirchhausen, 2009). Our observation is consistent with an alternative model in which clathrin first assembles a flat lattice, which subsequently rearranges into a curved one (den Otter and Briels, 2011; Heuser, 1989; Hoffmann et al., 2010; Traub, 2009). However, the transition from a flat to a curved clathrin lattice would require complex rearrangements of the lattice interactions, which are considered unlikely to occur (Kirchhausen, 2009). We therefore prefer a third model in which clathrin is recruited to the flat plasma membrane



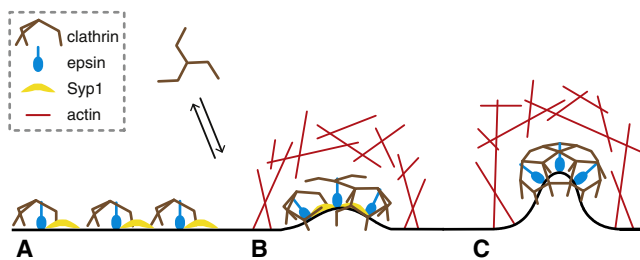


**Figure 6. A Schematic Model of Endocytic Membrane Bending, Clathrin Coat Arrangement, and Actin Polymerization**

(A) Early-arriving endocytic proteins, including clathrin (brown), the F-BAR domain protein Syp1 (yellow), and epsins (blue), have properties implicated in membrane bending. They are all present at the endocytic site before actin but are unable to induce membrane curvature. Clathrin is localized to the flat membrane but may not be assembled into a continuous lattice and is exchanging with the soluble pool.

(B) Bending of the plasma membrane begins only upon actin polymerization (red).

(C) Clathrin rearranges during invagination to form the assembled coat. A variation of this model, in which clathrin initially assembles a continuous lattice on the flat plasma membrane before rearranging into a curved lattice upon membrane bending, cannot be excluded but would require complex rearrangements of the lattice.

but does not directly assemble into a continuous oligomeric lattice (Figure 6). Rearrangement of clathrin into a continuous, curved lattice structure would occur subsequently, during the initial stages of actin-mediated membrane invagination. This is consistent with the finding that clathrin molecules undergo continuous rapid exchange at the endocytic site (Wu et al., 2001, 2003).

#### Amphiphysins Promote Elongation of the Invagination

After reaching 50 nm depth, further invagination growth proceeds by forming a parallel, tubular segment between the tip and the plasma membrane. In vitro, amphiphysins, like other N-BAR-containing proteins, are able to tubulate liposomes (Gallop et al., 2006; Qualmann et al., 2011; Youn et al., 2010), but how such proteins act on the membrane in vivo in the context of the dynamic endocytic machinery is less clear. We found that, in wild-type cells, Rvs167 is exclusively recruited to invaginations of at least 50 nm depth with parallel membrane segments and that parallel membranes can form before Rvs167 binding. In the *rvs167Δ* mutant, most invaginations were below 30 nm in depth. Because most endocytic sites proceed through scission in the *rvs167Δ* mutant, the presence of shallow invaginations suggests that endocytosis initiates normally but that elongation is hindered. Consistent with this, endocytic vesicles in the *rvs167Δ* mutant were smaller than in wild-type cells. A small fraction of the shallow invaginations may represent a previously observed minority retraction phenotype (Kaksonen et al., 2005; Kishimoto et al., 2011).

By EM, Kishimoto et al. (2011) reported a subtle 2 nm increase in width of endocytic invaginations and more frequent long invaginations in *rvs167Δ* cells. However, in our data set, the most dramatic difference was overrepresentation of short invaginations (<30 nm). These invaginations could be reliably identi-

fied with our correlative method but were not detected as endocytic sites in earlier studies. Based on the observation by live-cell imaging that *rvs167Δ* cells are more sensitive to Latrunculin A, Kishimoto et al. (2011) suggested that actin and BAR domain proteins act synergistically to drive invagination. This suggestion fits well with our direct observations of membrane shape when Rvs167 is bound. Our results imply that Rvs167 senses and binds parallel membrane segments and permits actin-driven elongation of the invagination by promoting or stabilizing tubular membrane formation. When *RVS167* is deleted, shallow invaginations accumulate.

#### Neck Constriction Likely Results from Distributed Forces

As N-BAR domain proteins are known to induce curvature and even fission, the amphiphysin module has been considered as a strong candidate for forming the neck-like constriction and thereby causing scission, either directly (Campelo et al., 2010; Gallop et al., 2006; Kishimoto et al., 2011) or indirectly by protecting the membrane from phosphatase activity and creating line tension (Liu et al., 2009). Scission occurs in the *rvs167Δ* mutant, implying that neck formation must occur transiently, but we did not observe *rvs167Δ* invaginations at depths at which necks form in wild-type cells, so we cannot directly assess how Rvs167 shapes the neck. In wild-type cells, we found that the neck forms at 1/3 of the invagination depth. It forms after Rvs167 recruitment to invaginations of 50 nm depth and before scission but is otherwise uncoupled from invagination depth. These results are consistent with models in which amphiphysins stabilize or shape tubular membrane segments, whereas distributed forces, perhaps including a combination of actin-driven pulling forces and turgor pressure, mediate constriction and eventual scission.

#### Scission Occurs at a Range of Invagination Depths and Defines the Vesicle Size Distribution

Because the appearance of a neck does not correlate with invagination depth, the question arises whether or not scission occurs at a particular invagination depth. The range of vesicle surface areas (Figure 4J) allows an estimate of what fraction of the invaginated membrane is incorporated into the vesicle and, thereby, where along each invagination the expected point of scission is positioned (the “future scission site”) (see [Extended Experimental Procedures](#)). We found that the future scission site leaves the plasma membrane plane when invaginations reach a depth of 60–80 nm and moves linearly inward with increasing invagination depth (Figure S5). We then calculated how the position of the future scission site relates to the position at 1/3 of the invagination depth at which neck constriction typically occurs. For a vesicle of average size, the future scission site is located at the neck position when the invagination is about 100 nm long. For the smallest vesicle, it is located at the neck position at an invagination depth of 70 nm, and for the largest vesicle, it is located at a depth of 130 nm. This range corresponds well to the range of invagination depths in which we observed necks (53–135 nm). Assuming the neck corresponds to the scission point, these data suggest that, in wild-type cells, neck formation and scission

can occur over a range of invagination depths from 70 to 130 nm and that this leads to the range of vesicle sizes observed.

### Three Key Functional Transitions of Endocytosis: Membrane Bending, Tubulation, and Constriction/Scission

Based on the ratios of vesicles and invaginations within different time windows, we found that scission occurs after 75% of time window 5 and after 59% of time window 6. Together, with the direct link between actin polymerization and membrane bending, this allows us to define three key functional transitions during the average endocytic event. At time point ( $T$ ) = 0 s, membrane curvature begins, correlating precisely with the start of Abp1 recruitment. On average, at  $T$  = 3 s, initial bending is completed, the invagination has a depth of  $\sim 50$  nm, tubulation begins, and Rvs167 is recruited. On average, at  $T$  = 9 s, 6 s after Rvs167 recruitment and with an average invagination depth of 100 nm, scission occurs.

### The Nascent Vesicle Is Elongated and Is Often Teardrop Shaped

We observed that vesicles have the shape of flattened spheres or rugby balls. This shape likely reflects the elongated, tubular shape of invaginations at the time point of scission. Provided that the endocytic membrane is not permeable, the vesicle will retain the surface-to-volume ratio of the elongated invagination. The variability in shape might be caused by forces exerted by the actin network, which could vary the length of the vesicle axes while the surface-to-volume ratio is maintained (Boukellal et al., 2004; Upadhyaya and van Oudenaarden, 2003). The plasma membrane relaxes back to a flat surface rapidly after scission, suggesting that the cytoskeleton is not constraining its shape.

### Actin Drives Inward Movement for the First 200 nm

Almost all of the observed vesicles were found within 200 nm of the plasma membrane, corresponding well to the 200 nm movement of internalized coat proteins seen by live-cell imaging (Kaksonen et al., 2003). Actin polymerization is thought to be nucleated at the base and neck of the invagination and to flow continuously from the membrane inward (Idrissi et al., 2008; Kaksonen et al., 2005). We therefore suggest that vesicles that have an actin network connected to the plasma membrane (which are found on average 116 nm from the plasma membrane) are still moving inward, propelled by continued actin polymerization or by actin network expansion due to relaxation. Vesicles whose actin network is disconnected from the plasma membrane (which are found on average 163 nm from the plasma membrane) have likely ceased to move inward and represent the final 1/3 of the lifetime of the vesicle-actin network assembly. The vesicles then remain within 200 nm of the plasma membrane, and further movement only occurs after depolymerization of the surrounding actin.

### The Entire Plasma Membrane Surface Is Internalized by Endocytosis in One Cell Cycle

The surface area of the vesicles was  $6,400 \text{ nm}^2 \pm 1,900 \text{ nm}^2$ , which represents the mean area of plasma membrane that is being internalized per endocytic event. Based on this number,

and considering an average number of 0.43 actin patches per fl of cell volume (Karpova et al., 1998) and an actin patch lifetime of 15 s (Kaksonen et al., 2003), we estimated that a yeast cell of about 5  $\mu\text{m}$  diameter internalizes its complete plasma membrane surface by endocytosis in about 100 min, corresponding to approximately one round of the budding yeast cell cycle.

### A Quantitative 4D Model of Endocytosis

We have integrated the data set into a model that describes the average endocytic event determined from distinct ultrastructural stages reconstructed by ET (Figure 7 and Movie S1). Recruitment of the coat to the endocytic patch occurs without inducing any change in membrane curvature. At  $T$  = 0 s, the actin module is recruited, and membrane bending begins. The membrane is bent into a dome-like invagination with a curvature of  $\sim 12$  nm radius and a depth of  $\sim 50$  nm. At that point, the first tubular segments appear between the highly curved tip and the plasma membrane, leading to Rvs167 recruitment. For the average endocytic site, this stage is reached after 3 s. Further invagination occurs by extension of the tubular segment, facilitated by Rvs167. A ribosome-free cytosolic zone formed by the actin network around invaginations precedes the elongating invagination by about 80 nm. A neck forms at a position of 1/3 of the invagination depth after Rvs167 binding but at a moment uncoupled from the stage of invagination elongation. On average, at  $T$  = 9 s and an invagination depth of 100 nm, scission occurs. The plasma membrane relaxes rapidly, leaving no detectable scission scar. The nonspherical vesicles often retain a teardrop shape reminiscent of the necked invagination. After about 2/3 of the vesicle's lifetime, which for the average endocytic site is reached 13 s after actin recruitment, actin polymerization ends, and the actin network disconnects from the plasma membrane. During the whole time of localization to the actin module, the vesicle remains constricted to a 200 nm zone at the plasma membrane and does not fuse with endosomes.

### Conclusions

The plasma membrane is both the substrate of and an integral part of the endocytic machinery. Endocytic proteins both sense and manipulate its curvature to drive invagination and scission. A detailed description of the changes in membrane shape during endocytosis has, however, been missing. Using a precise and sensitive correlative FM and EM approach, we have molecularly identified functional stages during endocytosis and imaged their ultrastructure in 3D by using ET. This large quantitative data set reveals the sequence of changes in membrane shape that occur during endocytosis and places them in the context of recruitment and disassembly of endocytic protein modules. Parameterization and analysis of the data provide answers to key mechanistic questions on the initiation of membrane bending, membrane constriction, scission, and the formation of endocytic vesicle shapes. The results provide the experimental basis for predictive mathematical models of endocytic membrane shaping.

### EXPERIMENTAL PROCEDURES

Sample preparation, FM, ET, and fiducial-based correlation procedure were performed as described previously (Kukulski et al., 2011). Briefly, yeast cells

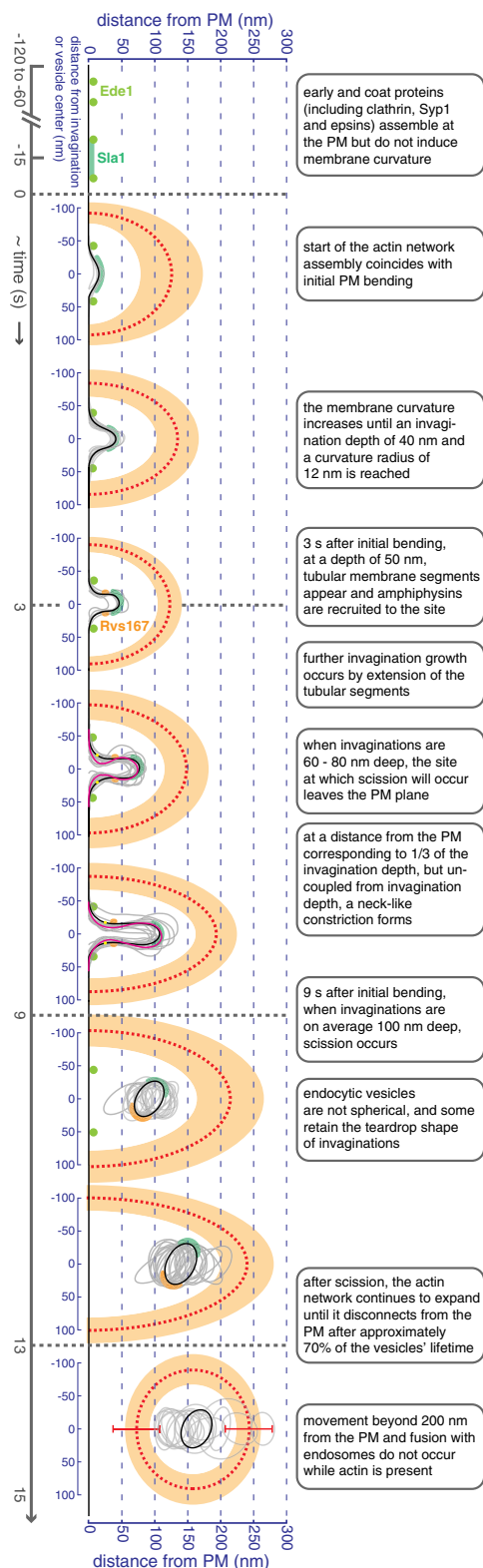


**Figure 7. A Quantitative 4D Model of Endocytosis**

Here, we visualize the sequence of ultrastructural stages during an average endocytic event by showing all endocytic profiles (gray outlines) grouped according to intermediate stage (see [Extended Experimental Procedures](#)),

were high-pressure frozen, freeze substituted, and embedded in Lowicryl. 300 nm resin sections placed on EM grids were imaged by FM prior to ET. Dual-axis tilt series were collected at a pixel size of 1.18 nm and at 1 degree increments. Lower magnification single-axis tilt series for fiducial-based correlation were collected at 2.53 nm pixel size and at 3 degree increments. Correlation of the fluorescent spots with coordinates of corresponding electron tomograms was performed by using fluorescent microspheres as a fiducial system. For a detailed description, see [Extended Experimental Procedures](#). For 5% of the targeted fluorescent signals, we found more than one endocytic event at the corresponding position in the electron tomogram. This is approximately the percentage expected by chance (see [Extended Experimental Procedures](#)), and these sites were excluded from the analysis.

### Extraction of Parameters for Analysis of Plasma Membrane Invaginations

The outlines of all invaginations were manually marked by clicking points using the EM Package in Amira ([Pruggnaller et al., 2008](#)) along the cytoplasmic leaflet of the plasma membrane within one oblique tomographic slice containing the long axis of the invagination, oriented with minimal deviation from the section plane. The sets of clicked points were aligned to each other and interpolated by using a local second-degree polynomial fit, resulting in 2D profiles of the invaginations. Parameters were extracted from the profiles. See also [Extended Experimental Procedures](#).

### Extraction of Parameters for Quantitative Analysis of Vesicles

The outlines and position of all vesicles were determined by manually clicking points using the EM package in Amira ([Pruggnaller et al., 2008](#)) on the cytoplasmic leaflet of the vesicle membrane within the tomographic volume. The contour and position of the plasma membrane near the vesicle were determined likewise. An ellipsoid fit was performed through the vesicle points, providing the coordinates of the vesicle center and a basis for parameter extraction. See also [Extended Experimental Procedures](#).

### Quantitative Description of Exclusion Zones

To quantify the ribosome-free cytoplasmic zone around endocytic invaginations and vesicles, we placed a hexagonal grid onto a projection of a series of tomographic slices and determined the hexagons around each endocytic site that did not contain ribosomes, as well as the hexagon enclosing the invagination tip or the center of the vesicle. See also [Extended Experimental Procedures](#).

### SUPPLEMENTAL INFORMATION

Supplemental Information includes Extended Experimental Procedures, five figures, and one movie and can be found with this article online at <http://dx.doi.org/10.1016/j.cell.2012.05.046>.

### ACKNOWLEDGMENTS

This study was technically supported by Frank Thommen and by the EMBL EM core facility. We thank Jan Ellenberg and François Nédélec for critical reading of the manuscript and Wolfgang Huber for statistical advice. W.K. acknowledges an EMBL interdisciplinary postdoctoral fellowship and a fellowship for advanced researchers from the Swiss National Science Foundation.

together with the average profiles of each stage (black outlines, magenta for invaginations with neck), as well as the average exclusion zone depth and width (red dashed arcs) with SDs (orange shading). Horizontal gray dashed lines indicate key functional transitions (see [Discussion](#)). Proteins are marked in light green (Ede1), dark green (Sla1), and orange (Rvs167). The future scission site is marked by yellow dots. The time scale is that of the average endocytic event. This data set can also be visualized as a movie ([Movie S1](#)).



Received: October 21, 2011

Revised: April 4, 2012

Accepted: May 17, 2012

Published: August 2, 2012

## REFERENCES

- Anderson, R.G.W., Brown, M.S., and Goldstein, J.L. (1977). Role of the coated endocytic vesicle in the uptake of receptor-bound low density lipoprotein in human fibroblasts. *Cell* 10, 351–364.
- Boettner, D.R., D'Agostino, J.L., Torres, O.T., Daugherty-Clarke, K., Uygun, A., Reider, A., Wendland, B., Lemmon, S.K., and Goode, B.L. (2009). The F-BAR protein Syp1 negatively regulates WASp-Arp2/3 complex activity during endocytic patch formation. *Curr. Biol.* 19, 1979–1987.
- Boettner, D.R., Chi, R.J., and Lemmon, S.K. (2012). Lessons from yeast for clathrin-mediated endocytosis. *Nat. Cell Biol.* 14, 2–10.
- Boukellal, H., Campás, O., Joanny, J.F., Prost, J., and Sykes, C. (2004). Soft Listeria: actin-based propulsion of liquid drops. *Phys. Rev. E Stat. Nonlin. Soft Matter Phys.* 69, 061906.
- Brodsky, F.M., Chen, C.Y., Knuehl, C., Towler, M.C., and Wakeham, D.E. (2001). Biological basket weaving: formation and function of clathrin-coated vesicles. *Annu. Rev. Cell Dev. Biol.* 17, 517–568.
- Campelo, F., Fabrikant, G., McMahon, H.T., and Kozlov, M.M. (2010). Modeling membrane shaping by proteins: focus on EHD2 and N-BAR domains. *FEBS Lett.* 584, 1830–1839.
- Carroll, S.Y., Stimpson, H.E., Weinberg, J., Toret, C.P., Sun, Y., and Drubin, D.G. (2012). Analysis of yeast endocytic site formation and maturation through a regulatory transition point. *Mol. Biol. Cell* 23, 657–668.
- Collins, A., Warrington, A., Taylor, K.A., and Svitkina, T. (2011). Structural organization of the actin cytoskeleton at sites of clathrin-mediated endocytosis. *Curr. Biol.* 21, 1167–1175.
- Conner, S.D., and Schmid, S.L. (2003). Regulated portals of entry into the cell. *Nature* 422, 37–44.
- Cureton, D.K., Massol, R.H., Whelan, S.P., and Kirchhausen, T. (2010). The length of vesicular stomatitis virus particles dictates a need for actin assembly during clathrin-dependent endocytosis. *PLoS Pathog.* 6, e1001127.
- den Otter, W.K., and Briels, W.J. (2011). The generation of curved clathrin coats from flat plaques. *Traffic* 12, 1407–1416.
- Ford, M.G.J., Mills, I.G., Peter, B.J., Vallis, Y., Praefcke, G.J.K., Evans, P.R., and McMahon, H.T. (2002). Curvature of clathrin-coated pits driven by epsin. *Nature* 419, 361–366.
- Galletta, B.J., Mooren, O.L., and Cooper, J.A. (2010). Actin dynamics and endocytosis in yeast and mammals. *Curr. Opin. Cell Biol.* 21, 604–610.
- Gallop, J.L., Jao, C.C., Kent, H.M., Butler, P.J.G., Evans, P.R., Langen, R., and McMahon, H.T. (2006). Mechanism of endophilin N-BAR domain-mediated membrane curvature. *EMBO J.* 25, 2898–2910.
- Henne, W.M., Boucrot, E., Meinecke, M., Evergren, E., Vallis, Y., Mittal, R., and McMahon, H.T. (2010). FCHo proteins are nucleators of clathrin-mediated endocytosis. *Science* 328, 1281–1284.
- Heuser, J. (1980). Three-dimensional visualization of coated vesicle formation in fibroblasts. *J. Cell Biol.* 84, 560–583.
- Heuser, J. (1989). Effects of cytoplasmic acidification on clathrin lattice morphology. *J. Cell Biol.* 108, 401–411.
- Hinrichsen, L., Meyerholz, A., Groos, S., and Ungewickell, E.J. (2006). Bending a membrane: how clathrin affects budding. *Proc. Natl. Acad. Sci. USA* 103, 8715–8720.
- Hoffmann, A., Dannhauser, P.N., Groos, S., Hinrichsen, L., Curth, U., and Ungewickell, E.J. (2010). A comparison of GFP-tagged clathrin light chains with fluorochromated light chains in vivo and in vitro. *Traffic* 11, 1129–1140.
- Idrissi, F.-Z., Grötsch, H., Fernández-Golbano, I.M., Presciatto-Baschong, C., Riezman, H., and Geli, M.-I. (2008). Distinct acto/myosin-I structures associate with endocytic profiles at the plasma membrane. *J. Cell Biol.* 180, 1219–1232.
- Itoh, T., Erdmann, K.S., Roux, A., Habermann, B., Werner, H., and De Camilli, P. (2005). Dynamin and the actin cytoskeleton cooperatively regulate plasma membrane invagination by BAR and F-BAR proteins. *Dev. Cell* 9, 791–804.
- Kaksonen, M., Sun, Y., and Drubin, D.G. (2003). A pathway for association of receptors, adaptors, and actin during endocytic internalization. *Cell* 115, 475–487.
- Kaksonen, M., Toret, C.P., and Drubin, D.G. (2005). A modular design for the clathrin- and actin-mediated endocytosis machinery. *Cell* 123, 305–320.
- Karpova, T.S., McNally, J.G., Moltz, S.L., and Cooper, J.A. (1998). Assembly and function of the actin cytoskeleton of yeast: relationships between cables and patches. *J. Cell Biol.* 142, 1501–1517.
- Kirchhausen, T. (2009). Imaging endocytic clathrin structures in living cells. *Trends Cell Biol.* 19, 596–605.
- Kishimoto, T., Sun, Y., Buser, C., Liu, J., Michelot, A., and Drubin, D.G. (2011). Determinants of endocytic membrane geometry, stability, and scission. *Proc. Natl. Acad. Sci. USA* 108, E979–E988.
- Kukulski, W., Schorb, M., Welsch, S., Picco, A., Kaksonen, M., and Briggs, J.A. (2011). Correlated fluorescence and 3D electron microscopy with high sensitivity and spatial precision. *J. Cell Biol.* 192, 111–119.
- Liu, J., Kaksonen, M., Drubin, D.G., and Oster, G. (2006). Endocytic vesicle scission by lipid phase boundary forces. *Proc. Natl. Acad. Sci. USA* 103, 10277–10282.
- Liu, J., Sun, Y., Drubin, D.G., and Oster, G.F. (2009). The mechanochemistry of endocytosis. *PLoS Biol.* 7, e1000204.
- McMahon, H.T., and Boucrot, E. (2011). Molecular mechanism and physiological functions of clathrin-mediated endocytosis. *Nat. Rev. Mol. Cell Biol.* 12, 517–533.
- Mulholland, J., Preuss, D., Moon, A., Wong, A., Drubin, D., and Botstein, D. (1994). Ultrastructure of the yeast actin cytoskeleton and its association with the plasma membrane. *J. Cell Biol.* 125, 381–391.
- Newpher, T.M., Smith, R.P., Lemmon, V., and Lemmon, S.K. (2005). In vivo dynamics of clathrin and its adaptor-dependent recruitment to the actin-based endocytic machinery in yeast. *Dev. Cell* 9, 87–98.
- Nixon, S.J., Webb, R.I., Floetenmeyer, M., Schieber, N., Lo, H.P., and Parton, R.G. (2009). A single method for cryofixation and correlative light, electron microscopy and tomography of zebrafish embryos. *Traffic* 10, 131–136.
- Perrais, D., and Merrifield, C.J. (2005). Dynamics of endocytic vesicle creation. *Dev. Cell* 9, 581–592.
- Peter, B.J., Kent, H.M., Mills, I.G., Vallis, Y., Butler, P.J.G., Evans, P.R., and McMahon, H.T. (2004). BAR domains as sensors of membrane curvature: the amphiphysin BAR structure. *Science* 303, 495–499.
- Pruggnaller, S., Mayr, M., and Frangakis, A.S. (2008). A visualization and segmentation toolbox for electron microscopy. *J. Struct. Biol.* 164, 161–165.
- Pucadyil, T.J., and Schmid, S.L. (2008). Real-time visualization of dynamin-catalyzed membrane fission and vesicle release. *Cell* 135, 1263–1275.
- Qualmann, B., Koch, D., and Kessels, M.M. (2011). Let's go bananas: revisiting the endocytic BAR code. *EMBO J.* 30, 3501–3515.
- Reider, A., Barker, S.L., Mishra, S.K., Im, Y.J., Maldonado-Báez, L., Hurley, J.H., Traub, L.M., and Wendland, B. (2009). Syp1 is a conserved endocytic adaptor that contains domains involved in cargo selection and membrane tubulation. *EMBO J.* 28, 3103–3116.
- Roth, T.F., and Porter, K.R. (1964). Yolk protein uptake in the oocyte of the mosquito *Aedes aegypti*. *L. J. Cell Biol.* 20, 313–332.
- Sirotkin, V., Berro, J., Macmillan, K., Zhao, L., and Pollard, T.D. (2010). Quantitative analysis of the mechanism of endocytic actin patch assembly and disassembly in fission yeast. *Mol. Biol. Cell* 21, 2894–2904.
- Stimpson, H.E.M., Toret, C.P., Cheng, A.T., Pauly, B.S., and Drubin, D.G. (2009). Early-arriving Syp1p and Ede1p function in endocytic site placement and formation in budding yeast. *Mol. Biol. Cell* 20, 4640–4651.
- Takagi, T., Ishijima, S.A., Ochi, H., and Osumi, M. (2003). Ultrastructure and behavior of actin cytoskeleton during cell wall formation in the fission yeast *Schizosaccharomyces pombe*. *J. Electron Microsc. (Tokyo)* 52, 161–174.

- Taylor, M.J., Perrais, D., and Merrifield, C.J. (2011). A high precision survey of the molecular dynamics of mammalian clathrin-mediated endocytosis. *PLoS Biol.* 9, e1000604.
- Toshima, J.Y., Toshima, J., Kaksonen, M., Martin, A.C., King, D.S., and Drubin, D.G. (2006). Spatial dynamics of receptor-mediated endocytic trafficking in budding yeast revealed by using fluorescent alpha-factor derivatives. *Proc. Natl. Acad. Sci. USA* 103, 5793–5798.
- Traub, L.M. (2009). Clathrin couture: fashioning distinctive membrane coats at the cell surface. *PLoS Biol.* 7, e1000192.
- Upadhyaya, A., and van Oudenaarden, A. (2003). Biomimetic systems for studying actin-based motility. *Curr. Biol.* 13, R734–R744.
- Wu, X., Zhao, X., Baylor, L., Kaushal, S., Eisenberg, E., and Greene, L.E. (2001). Clathrin exchange during clathrin-mediated endocytosis. *J. Cell Biol.* 155, 291–300.
- Wu, X., Zhao, X., Puertollano, R., Bonifacino, J.S., Eisenberg, E., and Greene, L.E. (2003). Adaptor and clathrin exchange at the plasma membrane and trans-Golgi network. *Mol. Biol. Cell* 14, 516–528.
- Yarar, D., Waterman-Storer, C.M., and Schmid, S.L. (2005). A dynamic actin cytoskeleton functions at multiple stages of clathrin-mediated endocytosis. *Mol. Biol. Cell* 16, 964–975.
- Youn, J.Y., Friesen, H., Kishimoto, T., Henne, W.M., Kurat, C.F., Ye, W., Ceccarelli, D.F., Sicheri, F., Kohlwein, S.D., McMahon, H.T., and Andrews, B.J. (2010). Dissecting BAR domain function in the yeast Amphiphysins Rvs161 and Rvs167 during endocytosis. *Mol. Biol. Cell* 21, 3054–3069.